2014

Buoyancy-Induced On-the-Spot Mixing in Droplets Evaporating on Non-Wetting Surfaces

S. Dash
Purdue University

A. Chandramohan
Purdue University

J A. Weibel
Purdue University, jaweibel@purdue.edu

S V. Garimella
Purdue University, sureshg@purdue.edu

Dash, S.; Chandramohan, A.; Weibel, J A.; and Garimella, S V., "Buoyancy-Induced On-the-Spot Mixing in Droplets Evaporating on Non-Wetting Surfaces" (2014). *CTRC Research Publications.* Paper 248.
http://dx.doi.org/10.1103/PhysRevE.90.062407

Buoyancy-induced on-the-spot mixing in droplets evaporating on nonwetting surfaces

Susmita Dash, Aditya Chandramohan, Justin A. Weibel, and Suresh V. Garimella*
School of Mechanical Engineering and Birck Nanotechnology Center, Purdue University, West Lafayette, Indiana 47907, USA
(Received 9 July 2014; revised manuscript received 19 October 2014; published 31 December 2014)

We investigate hitherto-unexplored flow characteristics inside a sessile droplet evaporating on heated hydrophobic and superhydrophobic surfaces and propose the use of evaporation-induced flow as a means to promote efficient "on-the-spot" mixing in microliter-sized droplets. Evaporative cooling at the droplet interface establishes a temperature gradient that induces buoyancy-driven convection inside the droplet. An asymmetric single-roll flow pattern is observed on the superhydrophobic substrate, in stark contrast with the axisymmetric toroidal flow pattern that develops on the hydrophobic substrate. The difference in flow patterns is attributed to the larger height-to-diameter aspect ratio of the droplet (of the same volume) on the superhydrophobic substrate, which dictates a single asymmetric vortex as the stable buoyancy-induced convection mode. A scaling analysis relates the observed velocities inside the droplet to the Rayleigh number. On account of the difference in flow patterns, Rayleigh numbers, and the reduced solid-liquid contact area, the flow velocity is an order of magnitude higher in droplets evaporating on a superhydrophobic substrate as compared to hydrophobic substrates. Flow velocities in all cases are shown to increase with substrate temperature and droplet size: The characteristic time required for mixing of a dye in an evaporating sessile droplet is reduced by ∼8 times on a superhydrophobic surface when the substrate temperature is increased from 40 to 60 °C. The mixing rate is ∼15 times faster on the superhydrophobic substrate compared to the hydrophobic surface maintained at the same temperature of 60 °C.

DOI: 10.1103/PhysRevE.90.062407 PACS number(s): 68.08.Bc, 47.55.nb, 47.55.P−, 64.70.fm

I. INTRODUCTION

Prediction and control of evaporation-driven convection patterns during droplet evaporation on nonwetting surfaces, and the resulting spatial distribution of particulate deposits on the surfaces, are crucial for application in crystal arrays [1], DNA microarrays [2], nanofabrication [3,4], and sensors [5–7]. These applications call for an improved understanding of the physics of flow inside an evaporating sessile droplet and its dependence on the substrate wetting properties, which can assist in the development of nonintrusive methods for manipulating flow inside microdroplets.

During droplet evaporation with a pinned contact line on hydrophilic surfaces, the nonuniform evaporative mass flux along the droplet interface results in capillary flow directed towards the contact line [8]. This results in a ringlike deposition pattern on the surface, also termed the "coffee-ring" effect [8], which is not desirable in applications that require a localized deposit [5,6,9]. Recirculating flow can be induced inside the droplet either by surface tension (Marangoni convection) [10–12] or buoyancy (Rayleigh convection) [13,14]. The direction of temperature gradient along the droplet interface, which determines the direction of surface-tension-driven recirculating flows, depends on fluid type, droplet size, and contact angle [8], as well as the ratio of substrate-to-liquid thermal conductivity [15] and even the shape of the particles inside the droplet [16]. While Marangoni convection has been theoretically predicted to occur in several fluids, its realization in water has not been consistently validated in experiments [10,12,17]. Suppression of Marangoni convection in water droplets is attributed to the large dipole moment of water molecules which attracts contamination on the free surface [10]. Buoyancy-driven Rayleigh-Bénard convection results either from a temperature- or concentration-induced density gradient inside the droplet [14].

The recirculating flow inside droplets can be used as a means for mixing and manipulation of particles. Efficient mixing is extremely important in various microfluidic devices for biological and chemical applications [18]. However, the low Reynolds numbers characteristic of microfluidic flows [19] render mixing of particles or solute in a microscale droplet challenging. In lab-on-a-chip devices, the rate of chemical reactions, which relies on mixing, is often limited by mass diffusion. Different mechanisms that achieve fast mixing by promoting chaotic advection include flow through irregularly winding channels [20], magnetic stirring [21], and acoustic excitation [22]. Obtaining on-the-spot mixing in stationary droplets is of significant importance to digital microfluidic systems, wherein alternative strategies that require movement of the droplet to enable mixing cannot be implemented. As one approach to on-the-spot mixing, convection arising from electrowetting-induced oscillation of a static droplet was recently reported to enhance mixing [23]. While the recirculating flow field in an evaporating droplet can be manipulated through modification of the surface wetting properties, this has never been previously investigated as a mixing enhancement method for digital microfluidics.

Surface wettability may be modified by altering the chemical composition and morphology of the surface. Low-wettability superhydrophobic surfaces, characterized by a high contact angle and low contact angle hysteresis, can be fabricated by careful engineering of surface roughness and by using low surface energy coatings [24,25]. The low contact angle hysteresis of smooth hydrophobic and structured superhydrophobic surfaces results in a predominant constant contact angle (CCA) mode during evaporation of a sessile droplet, wherein the contact angle remains almost constant and evaporative mass loss is manifested in the form of a receding

*Corresponding author: sureshg@purdue.edu

contact radius and reducing droplet height [26–28]. Extreme particulate localization can be achieved during evaporation on hydrophobic and superhydrophobic surfaces for biosensing [6] and self-assembly [29] applications. Localized deposition was reported during evaporation on superhydrophobic surfaces [30]; tuning of the surface geometry achieved a deposit size as small in area as 0.9% of the initial droplet base [30]. A quantitative estimate of the internal flow characteristics, and identification of the governing mechanism that establishes the flow field inside droplets evaporating on nonwetting surfaces, are needed to understand their relationship with the localized deposition pattern realized. While the flow pattern inside droplets evaporating on hydrophilic surfaces has been extensively studied [8,10], the literature on flow behavior inside droplets evaporating in a constant contact angle mode on nonwetting surfaces is limited [31].

The present work is a quantitative experimental demonstration of the flow pattern inside a droplet evaporating on a hydrophobic and a superhydrophobic surface. The results shed light on the dependence of flow characteristics inside an evaporating droplet on the substrate wettability, substrate temperature, and the droplet aspect ratio. The dependence of the flow velocity in the droplet on the thermal Rayleigh number, as a function of instantaneous volume and substrate temperature, is used to explain the forces that govern the convection patterns. The convective flow observed in droplets evaporating on superhydrophobic surfaces is assessed as a means to achieve efficient on-the-spot droplet mixing.

II. MATERIALS AND METHODS

The superhydrophobic substrate used in the experiments is fabricated with silicon prime wafers using standard lithography and dry etching (deep reactive-ion etch) techniques. The surface has a square array of pillars; the pitch of the pillars is $\sim 30\,\mu$m, the width of the tops of the pillars $\sim 10\,\mu$m, and the height of the pillars $\sim 20\,\mu$m. The textured surfaces were coated with Teflon ($\sim$50 nm thickness) to render them superhydrophobic. The hydrophobic substrate is a smooth Teflon-coated silicon wafer. The initial contact angle (CA) of the droplet on the hydrophobic and superhydrophobic substrates is 118 ± 2 and 157 ± 2 deg, respectively; the contact angle hysteresis on both surfaces is $\sim$10 deg.

In the experiments a deionized water droplet of $\sim 3\,\mu$l initial volume is allowed to evaporate on the substrate placed inside a transparent enclosure to avoid disturbance due to ambient air currents. The experiments are conducted on a hot stage that consists of a copper block that is electrically heated from the underside by a 10 W polyimide film heater; the sides of the block are insulated using fused ceramic foam. The sample substrate is attached to the top of the copper block with a uniform layer of thermally conductive silicone paste (Omegatherm 201, Omega). The temperature distribution within the copper block is measured throughout each test using a rake of thermocouples. A PID controller (TOT-1200, Temp-o-Trol) is used to regulate the heater power input to achieve a desired set-point temperature at the thermocouple nearest the substrate. The measured temperature variation across the height of the copper block is negligible; hence, the temperature nearest the sample substrate is quoted as the sample temperature for all the experiments. Experiments are conducted at three different substrate temperatures: 40 ± 0.5, 50 ± 0.5, and $60 \pm 0.5\,^{\circ}$C. The ambient temperature and humidity are maintained at $24 \pm 1\,^{\circ}$C and $36 \pm 3\%$, respectively. The water droplet is seeded with 1-μm-diameter fluorescent polystyrene microspheres with peak excitation and emission at 532 and 602 nm, respectively. A continuous diode-pumped solid-state Nd:YAG laser (Coherent Verdi V5; 532 nm) along with a Galilean lens arrangement is used to produce a light sheet of thickness $\sim 30\,\mu$m and height ~ 6 mm that illuminates the vertical central plane of the droplet. A laser power of 1 W is used in the experiments. Water has a very low absorption coefficient at the laser wavelength [32]; hence, laser-induced heating of water during the experiment is negligible. A high-speed camera (Photron FASTCAM 1024PCI) fitted with a microscope lens (Keyence VH-Z50L) and a high-pass filter (center wavelength = 620 nm, bandwidth = 52 nm) captures the light emitted from the seeding particles at 60 frames per second at a spatial resolution of $\sim 3.8\,\mu$m/pixel. Figure 1 shows a schematic diagram of the experimental setup. A modified lens arrangement is used for visualization of the horizontal cross-sectional plane of the droplet. All experimental results presented are acquired during the constant contact angle mode of evaporation, during which the mass loss due to evaporation results in a corresponding continual reduction in the height and contact radius of the droplet.

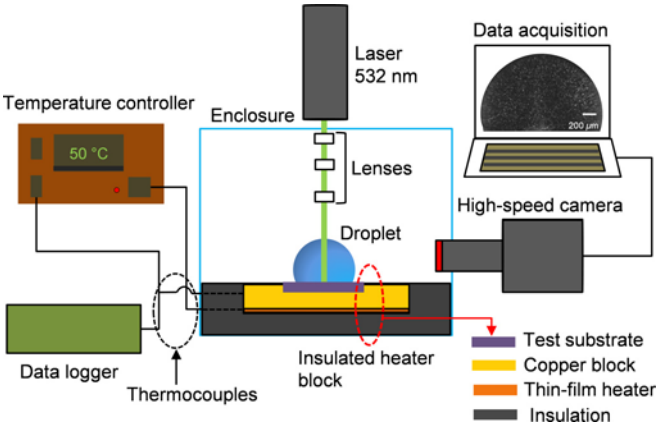

FIG. 1. (Color online) Experimental setup for flow visualization.

The particle image velocimetry vector field is computed using a multipass, cross-correlation algorithm with first- and second-pass window sizes of 32×32 and 16×16 pixels, and 50% overlap between consecutive frames. The instantaneous vector fields at each grid location are time averaged over a droplet volume change of $\pm 0.1\,\mu$l to obtain a reported vector field inside the droplet corresponding to a given volume. The "lens effect" of the spherical cap-shaped liquid droplet results in distortion of the velocity vectors: the vectors are severely compressed at the periphery (resulting in loss of vector data) and magnified at the center of the droplet [13]. A velocity-correction algorithm [13,33] is employed to correct for this distortion and to obtain an accurate quantitative estimate of the flow field (per details provided in Appendix A).

III. RESULTS AND DISCUSSION

A. Flow behavior during droplet evaporation on a hydrophobic substrate

Figures 2(a) and 2(b), respectively, show streaklines in the vertical and horizontal planes of a droplet at an instantaneous volume of 2 μl on the hydrophobic substrate maintained at 50 °C, obtained by superposing multiple sequential images. The corresponding velocity field at the central vertical plane of the droplet is shown in Fig. 2(c). A cross section of the toroidal vortex, appearing as a counter-rotating vortex pair in the 2D plane, is observed with flow directed inward towards the center of the droplet along the substrate and upward along the vertical axis. This flow behavior is opposite to that on a hydrophilic surface where the flow along the substrate is directed outwards towards the contact line [2,10]. The axisymmetric nature of the toroidal vortex pattern is further confirmed by PIV visualization in the horizontal plane of the droplet at its maximum diameter (at $y/h \approx 0.23$, where y and h represent the distance from the base of the droplet and the droplet height, respectively), as shown in Fig. 2(d).

Earlier studies have attributed the recirculating flow inside an evaporating droplet to the Marangoni convection caused by a surface tension gradient along the interface [10,16]. The temperature gradient along the surface of the droplet, which determines the direction of the Marangoni flow, is dependent on the geometry and the thermophysical properties of the droplet and substrate. If Marangoni convection were important in our experiments (CA □ 110 deg and substrate-to-droplet thermal conductivity ratio $k_R > 250$), the flow would be directed outward along the solid-liquid interface towards the contact line and downward along the vertical axis [10,15,34]. Instead, the observed upward direction of flow along the vertical axis indicates that the driving parameter here is the density gradient caused by the temperature stratification in the droplet, i.e., buoyancy-induced Rayleigh convection.

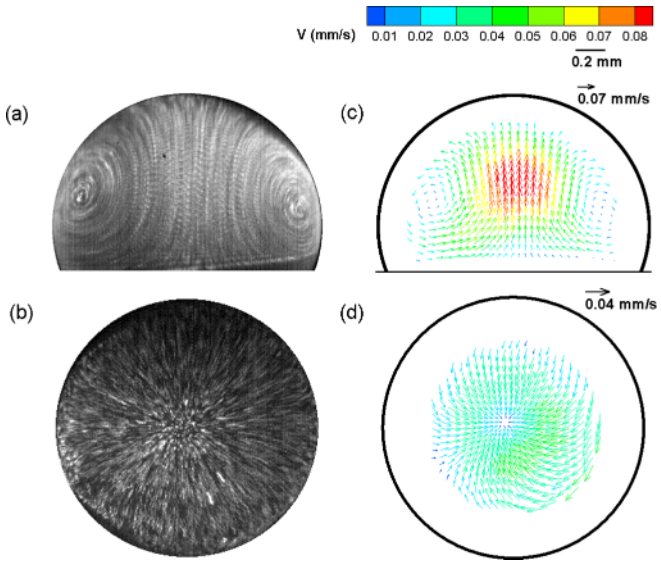

FIG. 2. (Color online) Flow field inside a droplet evaporating on a hydrophobic surface maintained at 50 °C at an instantaneous volume of 2 μl. Streaklines are visualized by superimposing multiple sequential (a) side-view images and (b) top-view images. Velocity vector maps of the (c) central vertical plane and (d) horizontal plane are shown.

A significant temperature drop is sustained along the height of an evaporating droplet resting on a hydrophobic surface (which supports a large contact angle) due to evaporative cooling at the interface [35]. The liquid nearer the substrate is at a higher temperature and lower density compared to the liquid at the top of the droplet. This results in an unstable equilibrium: the denser liquid at the top descends while the lighter liquid at the bottom ascends, and this global motion within the droplet leads to a three-dimensional toroidal vortex pattern. The absence of the outward capillary flow along the substrate—seen with hydrophilic surfaces—is attributed to the unpinned contact line and reduced evaporative flux near the contact line compared to droplets with an acute contact angle [27].

The strength of the buoyancy forces that drive the recirculating flow inside the droplet can be assessed using the Rayleigh number given by $\mathrm{Ra} = \frac{\rho g \beta}{\mu \alpha} \Delta T L^3$, where ρ and β are the density and thermal expansion coefficient of the liquid, respectively. The Rayleigh number decreases as the height of the droplet decreases, resulting in a lowered buoyancy-induced convection velocity at lower volumes, as shown in Fig. 3. The velocity field behavior with decreasing volume is consistent across all the substrate temperatures considered. The driving buoyancy force increases with an increase in the substrate temperature [28]. To illustrate the increase in flow velocity at higher substrate temperatures, the velocities extracted along the central vertical axis of the droplet at an instantaneous volume of 2 μl and at different substrate temperatures are shown in Fig. 4(a). The Rayleigh number corresponding to the different experiments on the hydrophobic substrate is evaluated. The temperature drop ΔT along the droplet height during evaporation is evaluated using a simple diffusion model [28]; details of the calculations are included in Appendix B. The present study establishes a direct correlation between the flow velocity inside droplets evaporating on heated hydrophobic surfaces and the Rayleigh number. Figure 4(b) shows that the maximum velocity inside the droplet, across all experiments, corresponding to substrate temperatures from 40 to 60 °C, and droplet volumes of 1.2 to 2 μl, is linearly related to the Rayleigh number. The flow velocity inside the droplet increases with an increase in Rayleigh number and signifies the dominance of buoyancy forces in water droplets on surfaces which support a large contact angle.

B. Flow behavior during droplet evaporation on a superhydrophobic substrate

Unlike the axisymmetric, toroidal flow pattern realized on a hydrophobic surface as discussed above, a single-roll asymmetric vortex, akin to the solid body rotation of a sphere, is observed inside the droplet evaporating on a superhydrophobic surface, as sketched in Fig. 5(a). The asymmetric vortex observed in droplets on the superhydrophobic surface is also in stark contrast to the axisymmetric fluid motion observed on hydrophilic [10] substrates in the literature. Since the flow is not axisymmetric, the relative orientation of the visualization plane with respect to the axis of the convection roll determines the velocity profile obtained during experimental measurement; all two-dimensional visualizations of central

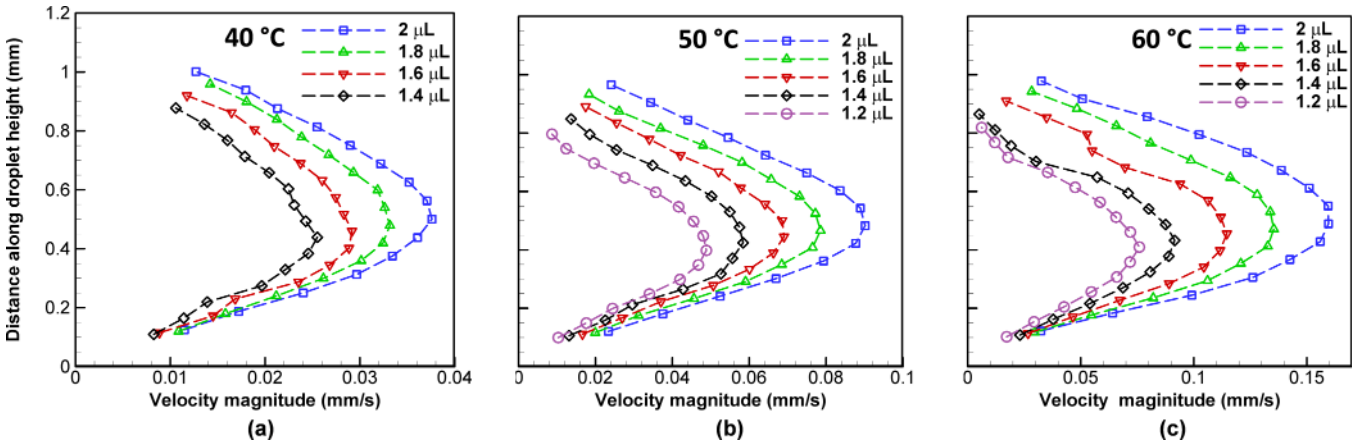

FIG. 3. (Color online) Variation of flow velocity on the hydrophobic substrate with changing volume of the evaporating droplet along its vertical axis of symmetry, corresponding to substrate temperatures of (a) 40 °C, (b) 50 °C, and (c) 60 °C.

vertical planes presented herein are near perpendicular to the rolling axis [as illustrated in Fig. 5(a)]. Figures 5(b) and 5(c) show the streaklines obtained by superposing multiple images in the vertical and horizontal planes, respectively. The horizontal cross section is visualized at a plane corresponding to the maximum diameter of the droplet (at $y = 0.46h$). The vector map in the vertical plane of the droplet at a substrate temperature of 50 °C is shown in Fig. 5(d). This flow pattern is consistent across all experiments conducted at the different substrate temperatures. The full, three-dimensional single-roll flow pattern can be qualitatively observed in the videos provided as Supplemental Material [36]. The velocity vector plot in the horizontal plane [Fig. 5(e)] shows that the flow pattern has one central, vertical plane of symmetry aligned with the direction of flow rotation [indicated by a solid black outline in Fig. 5(a)]; the horizontal, in-plane velocities are significantly lower compared to the velocity magnitudes in the central vertical plane [Fig. 5(d)].

The temperature differential along the height of the droplet is expected to be greater for a superhydrophobic surface, as compared to a hydrophobic substrate, due to its larger height-to-contact diameter ratio which leads to a longer conduction path between the smaller substrate contact area and the interface at the top of the droplet. Therefore, the flow pattern established in a water droplet evaporating on a superhydrophobic surface is also governed by buoyancy forces. The stark differences in the three-dimensional steady flow pattern in the droplets between the hydrophobic and superhydrophobic cases are attributed to the dependence of the primary instability mode of Rayleigh-Bénard convection on the geometry of the spherical cap droplet. The convection pattern resulting from the Rayleigh-Bénard instability in the presence of thermal buoyancy forces is dependent on the geometry of the system and the boundary conditions [37,38]. The threshold for attaining an asymmetric flow state in cylindrical prisms by Rayleigh-Bénard convection was previously

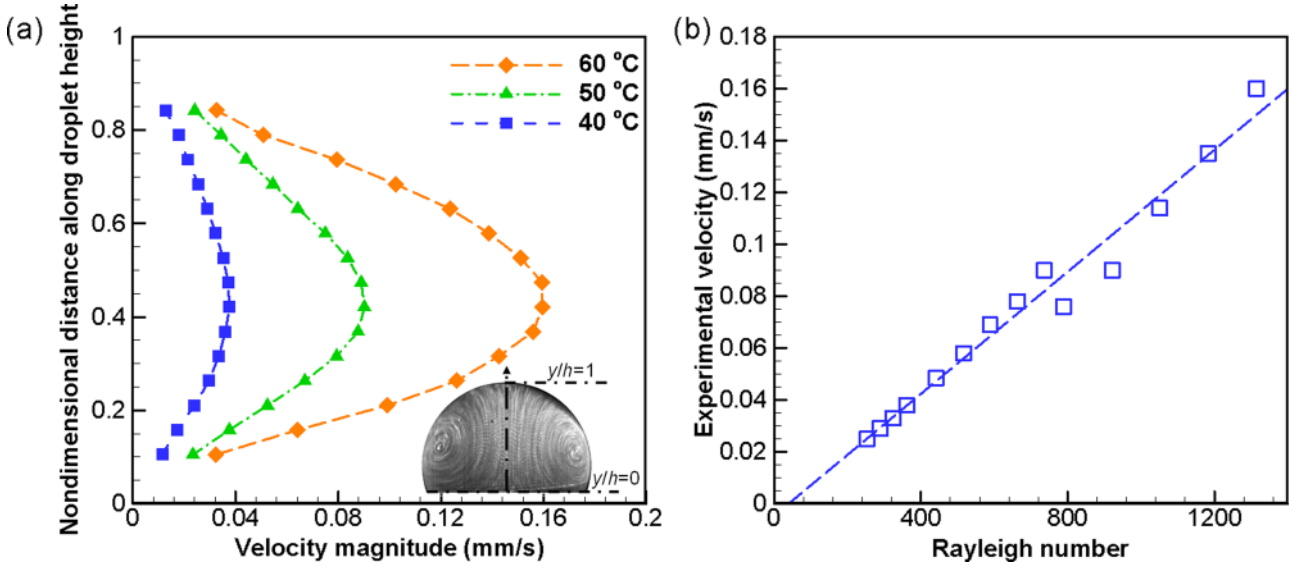

FIG. 4. (Color online) (a) Velocity magnitude along the vertical axis of symmetry of the droplet at a volume of 2 μl on the hydrophobic surface. (b) Variation of the maximum velocity inside the droplet at different substrate temperatures and volume, with respect to Rayleigh number.

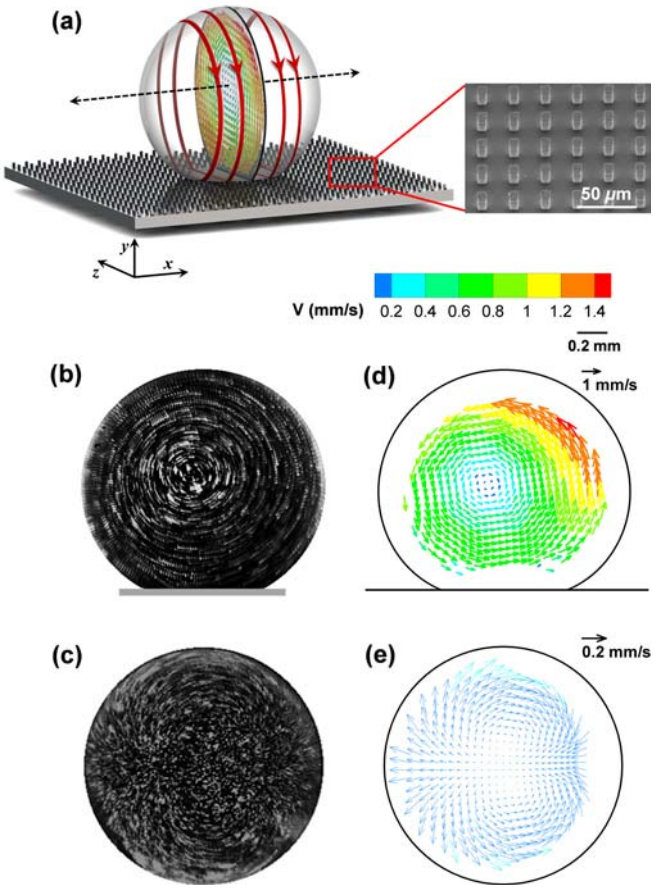

FIG. 5. (Color online) (a) Schematic sketch of the flow pattern observed inside a droplet evaporating on a superhydrophobic substrate maintained at 50 °C. The inset shows an SEM image of the superhydrophobic surface used in the experiments. Streaklines are visualized by superposing multiple sequential (b) side-view images and (c) top-view images. Velocity vector maps of the central (d) vertical plane and (e) horizontal plane.

established experimentally and numerically [37–39]. These studies showed that the form of the stable flow structure which emerges due to Rayleigh-Bénard convection is dependent on the cylinder aspect ratio (AR $= h/D$; where h is the height of the cylinder and D is the base diameter) and the Rayleigh number [37–39]. For a cylinder heated on end, a nonlinear numerical analysis of convection by Neumann [39] showed that stable axisymmetric toroidal vortex solutions are restricted to aspect ratios less than 0.72 depending on the wall boundary condition [38,39]. For a cylindrical geometry with aspect ratio □ 1, a one-roll mode was reported [37–39]. While these specific thresholds apply to flow in cylinders, the convection instability for low Rayleigh number flows inside spherical-cap droplets follows a similar behavior; this is supported by our experimental results for hydrophobic and superhydrophobic substrates. On the hydrophobic substrate (CA = 110 deg), the lower aspect ratio droplet ($h/D = 0.67$, where D is the droplet diameter) exhibits a stable axisymmetric flow. Conversely, on the superhydrophobic surface (CA = 150 deg), the higher aspect ratio ($h/D = 0.93$) leads to a stable single rotating vortex. Furthermore, the flow structure in the horizontal central plane [Fig. 5(e)] is analogous to the Rayleigh-Bénard instability-induced flow field with a one-roll mode observed in the horizontal cross section of cylindrical geometries with an aspect ratio of ∼1 [38]. The finding of an asymmetric convection pattern has particular significance to modeling approaches, which have routinely assumed an axisymmetric 2D droplet evaporation behavior [35].

The experiments on the superhydrophobic substrate reveal an identical vertical distance of the vortex center above the substrate across all substrate temperatures. When viewing along the rolling axis, it is observed that irrespective of the substrate temperature, the vortex center lies at a vertical height of 0.72 ± 0.02 mm from the base of the droplet for a 2 μl droplet. This corresponds to a nondimensional height $y/h = 0.496 \pm 0.015$. In the case of a droplet evaporating on a hydrophobic surface, the nondimensional height of the maximum velocity location, corresponding to the center of the toroidal convection pattern was observed at a nondimensional height $y/h \approx 0.4$ (Fig. 4). This nondimensional height remained unchanged for different instantaneous droplet volumes and surface temperatures on the hydrophobic substrate. The physical characteristics of the vortex structures in droplets on the hydrophobic and superhydrophobic substrates show that the vortex center of the flow pattern is constant for a given surface wettability.

The maximum velocity in the droplet evaporating on the superhydrophobic surface is on the order of 1000 μm/s. This flow velocity is an order of magnitude higher than is realized on the hydrophobic substrate, which is on the order of 100 μm/s. The higher evaporation-induced velocity in the case of the superhydrophobic surface is particularly noteworthy since the rate of evaporation is lower than for the hydrophobic surface [28]. The high recirculation velocity can be related to the higher Rayleigh number and the different flow pattern structure compared to a hydrophobic substrate. In addition, the solid-liquid contact area is ∼38 times smaller in the case of a superhydrophobic surface as compared to a hydrophobic surface which results in lower dissipative losses. The velocity magnitude inside the droplet increases with an increase in substrate temperature (Fig. 6). The rate of evaporation increases with substrate temperature, thereby increasing the extent of evaporative cooling, and the resulting temperature difference ΔT across the droplet. The recirculating flow behavior inside the droplet during evaporation on hydrophobic and superhydrophobic surfaces in conjunction with the sliding droplet contact line explains the localized evaporative deposition of particulate inclusions on such surfaces [28,30].

C. Evaporative-flow-induced mixing in droplets

We propose that the intense recirculation inside a droplet evaporating on a superhydrophobic surface may be exploited in microfluidic devices to achieve efficient mixing in microliter-sized droplets. Under species-diffusion-dominated conditions, the time required to homogenize a solution is dependent on the diffusion time scale $\tau_d = r^2/D$, where r is the radius of the drop and D is the diffusion coefficient. For a fluorescent dye (Rhodamine 6G; diffusion coefficient in water $= 4.14 \times 10^{-10}$ m^2/s [40]) mixing into a water droplet of volume ∼2 μl, the diffusion time scale is ∼24 min. The time scale for

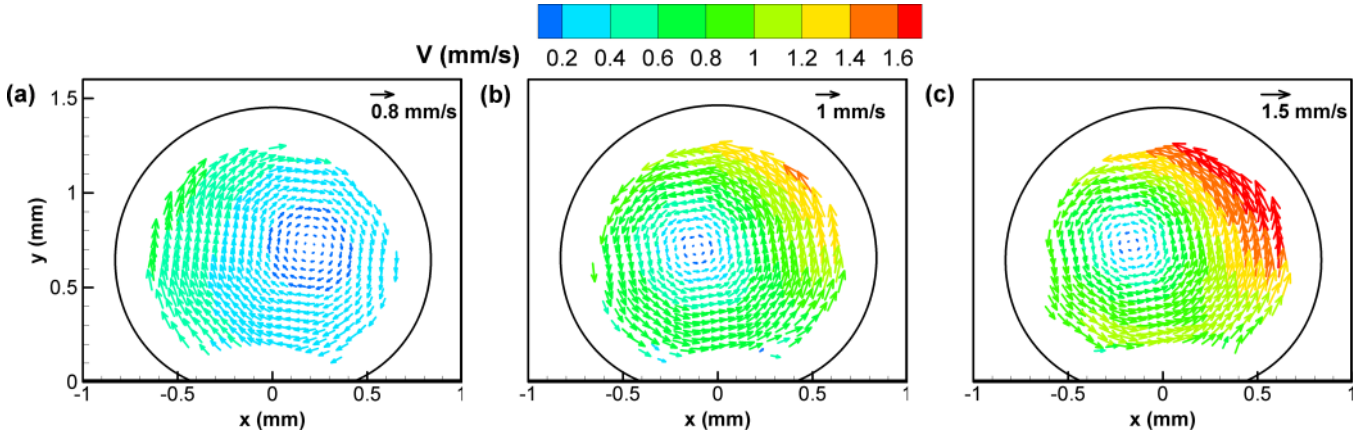

FIG. 6. (Color online) Velocity vectors in the central vertical plane of the droplet corresponding to superhydrophobic substrate temperatures of (a) 40 °C, (b) 50 °C, and (c) 60 °C.

mixing due to evaporative recirculation inside the droplet, on the other hand, can be estimated as $\tau_{\text{circ}} = n\,(2\pi/\omega)$, where ω is the angular velocity of the flow pattern and n is the number of rotations required for mixing. The angular velocity inside the droplet evaporating on a superhydrophobic surface increases with an increase in substrate temperature: $\omega = 0.75 \pm 0.10$, 1.71 ± 0.28, and $2.21 \pm 0.33\,\text{s}^{-1}$ corresponding to $T_{\text{sub}} = 40$, 50, and 60 °C, respectively. The corresponding mixing time scale reduces with this increase in the angular velocity, and should be on the order of seconds, depending on the number of rotations required for mixing.

The more efficient mixing on the superhydrophobic substrate with an increase in substrate temperature is demonstrated by proof-of-concept mixing experiments using fluorescent dye Rhodamine 6G (Fig. 7); movie files visualizing dye mixing

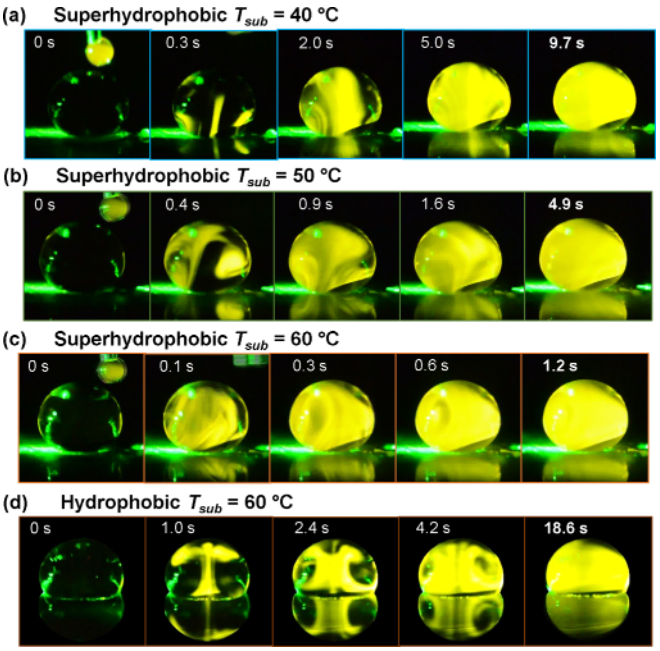

FIG. 7. (Color online) Time series images demonstrating dye mixing in an evaporating droplet on a superhydrophobic substrate maintained at (a) 40 °C, (b) 50 °C, (c) 60 °C, and on (d) hydrophobic substrate maintained at 60 °C.

are included as Supplemental Material [36]. The droplet volume used in the mixing experiments is ~10 μl for easier visualization. The evaporative flow field inside the droplet undergoes multiple rotations (on the order of ten) to realize complete mixing within the droplet. On the superhydrophobic substrate, the mixing time reduces by a factor of 8 from ~9.7 s at 40 °C to ~1.2 s at 60 °C. This convection-aided mixing time is two to three orders of magnitude less than the species-diffusion mixing time scale (~72 min for a 10 μl droplet), as anticipated from the scaling analysis which was based on velocity measurements in 2 μl droplets. At a fixed substrate temperature of 60 °C, the mixing time is reduced by ~15 times during droplet evaporation on the superhydrophobic substrate compared to the hydrophobic substrate (Fig. 7). Since the rate of evaporation of water droplets on superhydrophobic surfaces is low [28], efficient mixing can be obtained without much loss of mass within a short time period.

IV. CONCLUSION

The internal flow field of a droplet evaporating on heated hydrophobic and superhydrophobic surfaces is quantitatively mapped. The presence of an axisymmetric, toroidal vortex structure with flow directed upwards along the vertical axis, at a velocity directly correlated to the Rayleigh number, establishes the dominance of buoyancy-induced flow in a droplet evaporating on a hydrophobic substrate. The starkly different asymmetric evaporative flow pattern on superhydrophobic surfaces is attributed to the geometric effect of the high-aspect-ratio droplets on the buoyancy-driven convection. The flow velocity is an order of magnitude higher in the droplet on the superhydrophobic substrate than that observed on the hydrophobic substrate. This illustrates the potential for droplet evaporation on superhydrophobic surfaces to achieve more efficient droplet mixing for microfluidics applications; mixing is shown to be enhanced by ~15 times compared to on a hydrophobic substrate maintained at the same temperature.

ACKNOWLEDGMENT

Funding from the National Science Foundation for this work as a Fundamental Research Supplement to the Cooling

Technologies Research Center at Purdue University is gratefully acknowledged.

APPENDIX A: VELOCITY CORRECTION

A velocity-correction algorithm is applied to the acquired PIV vector field to account for optical distortion induced by the spherical droplet interface. The velocity mapping algorithm proposed by Kang *et al.* [13] is used with the correction reported by Minor *et al.* [33] incorporated. The ray-tracing method calculates the actual position of the particles based on the surface curvature and index of refraction of the liquid droplet. The ray tracing is realized by projecting the particle position, obtained from the captured image on the camera, onto the surface of the droplet by assuming that the droplet has a spherical profile. Based on the refractive indices of air and water, the surface projection is traced to the center plane of the droplet to determine the actual (i.e., corrected) particle position using Snell's law. The velocity vector correction is obtained by taking the derivative of the position correction [13]. The velocity field correction algorithm requires geometric characterization of the droplet contact radius, height, and the coordinates of the center of the base contact area, which are determined from the experimental images. Using an in-house image processing code developed in MATLAB (The Mathworks Inc., Natick, MA), the droplet image noise is reduced and the reflections removed. Subsequently the image is binarized and a boundary detection algorithm is used to determine the droplet profile, from which the geometric parameters of the droplet are estimated.

Figure 8 shows the vector plot in the central plane of droplets evaporating on hydrophobic and superhydrophobic substrate, before and after correction of vector position and magnitude. At the center of the visualization plane for the droplet placed on the hydrophobic substrate, the lens effect artificially expands the positions and increases the magnitudes of the vectors, for example, by approximately 34% at 50 °C [Fig. 8(a)]. Vector positions near the interface are heavily compressed toward the interface, ultimately resulting in a loss of information in this region even after correction [13]. The shifted vectors produced by the correction algorithm allow for identification of the actual position of the vortex center in the plane of visualization [Figs. 8(b) and 8(d)]. The uncertainty in determination of the corrected vectors is dependent on the errors in the measurement of the droplet contact radius, height, and center of the base contact area, which are each estimated to be within 1 pixel. The root-sum-squared approach was taken to assess this uncertainty, which was found to be within 2 μm/s.

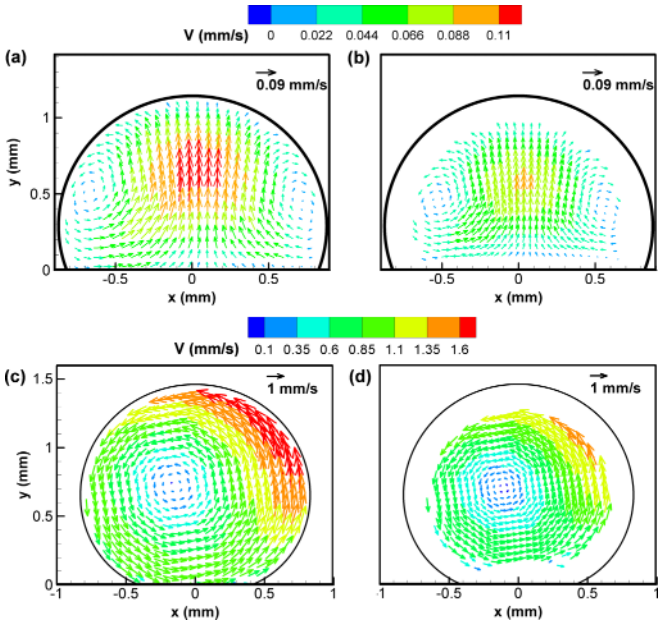

FIG. 8. (Color online) Velocity vectors in a droplet of volume 2 μl evaporating on a hydrophobic surface (a) before and (b) after velocity correction and on a superhydrophobic surface (c) before and (d) after velocity correction; the substrates are maintained at 50 °C.

APPENDIX B: DIFFUSION MODEL

The contribution of buoyancy to the flow behavior inside the droplet evaporating on a hydrophobic substrate is assessed in terms of the Rayleigh number. A quantitative determination of Rayleigh number requires an estimation of the temperature drop ΔT along the droplet height. In the present study a simple diffusion model [28] is used to determine the temperature drop along the droplet height during evaporation. In order to use the simplified model, the Peclet number—a measure of the relative importance of advective and diffusive transport—must be calculated to ensure that thermal diffusion across the droplet is the dominant mode of heat transfer for the substrate temperatures considered here. The Peclet number is defined as $\mathrm{Pe} = UL/\alpha$, where U, L, and α represent the characteristic velocity, length scale, and thermal diffusivity of the droplet, respectively. Using the average velocity in the vertical plane of the droplet as the representative flow velocity (U), and the height of the droplet as the length scale, a representative value for Pe corresponding to each different instantaneous droplet volume is determined. Figure 9 shows the Peclet number corresponding to different instantaneous droplet volumes and hydrophobic substrate temperatures. The

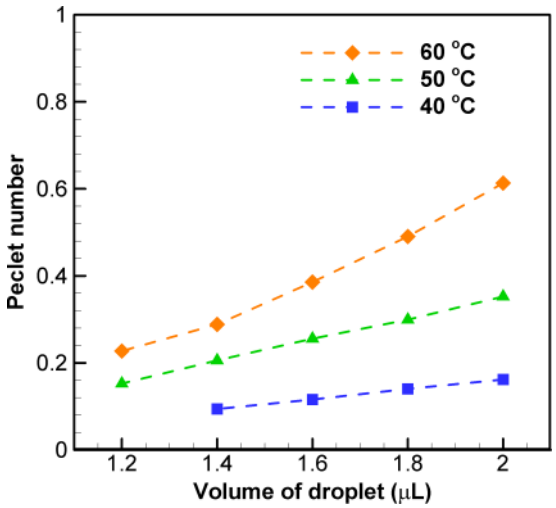

FIG. 9. (Color online) Peclet number at different instantaneous droplet volumes corresponding to different surface temperatures for a hydrophobic substrate.

Peclet numbers thus obtained are typically less than 1 for the substrate temperatures considered. It is therefore appropriate to assume thermal diffusion to be the primary mode of heat transfer in a reduced-order model for the temperature field. Using the diffusion model [28], the temperature drops along the droplet height are determined to be 7.1, 11.0, and 15.9 °C, corresponding to respective substrate temperatures of 40, 50, and 60 °C. The thermophysical properties are evaluated at the average temperature of the droplet obtained from the solution of the diffusion-only model [28].

[1] B. Su, S. Wang, J. Ma, Y. Song, and L. Jiang, Adv. Funct. Mater. **21**, 3297 (2011).

[2] G. Ciasca, L. Businaro, M. Papi, A. Notargiacomo, M. Chiarpotto, A. D. Ninno, V. Palmieri, S. Carta, E. Giovine, A. Gerardino, and M. D. Spirito, Nanotechnology **24**, 495302 (2013).

[3] W. Xu, R. Leeladhar, Y.-T. Tsai, E.-H. Yang, and C.-H. Choi, Appl. Phys. Lett. **98**, 073101 (2011).

[4] M. Maeki, H. Yamaguchi, K. Yamashita, H. Nakamura, M. Miyazaki, and H. Maeda, Chem. Commun. **48**, 5037 (2012).

[5] J. T. Wen, C.-M. Ho, and P. B. Lillehoj, Langmuir **29**, 8440 (2013).

[6] F. D. Angelis, F. Gentile, F. Mecarini, G. Das, M. Moretti, P. Candeloro, M. L. Coluccio, G. Cojoc, A. Accardo, C. Liberale, R. P. Zaccaria, G. Perozziello, L. Tirinato, A. Toma, G. Cuda, R. Cingolani, and E. D. Fabrizio, Nat. Photon. **5**, 682 (2011).

[7] A. Ebrahimi, P. Dak, E. Salm, S. Dash, S. V. Garimella, R. Bashir, and M. A. Alam, Lab. Chip **13**, 4248 (2013).

[8] R. D. Deegan, O. Bakajin, T. F. Dupont, G. Huber, S. R. Nagel, and T. A. Witten, Phys. Rev. E **62**, 756 (2000).

[9] A. Ressine, D. Finnskog, G. Marko-Varga, and T. Laurell, NanoBiotechnology **4**, 18 (2008).

[10] H. Hu and R. G. Larson, Langmuir **21**, 3972 (2005).

[11] H. Ghasemi and C. A. Ward, Phys. Rev. Lett. **105**, 136102 (2010).

[12] R. Savino and S. Fico, Phys. Fluids **16**, 3738 (2004).

[13] K. H. Kang, S. J. Lee, C. M. Lee, and I. S. Kang, Meas. Sci. Technol. **15**, 1104 (2004).

[14] B. Trouette, E. Chénier, F. Doumenc, C. Delcarte, and B. Guerrier, Phys. Fluids **24**, 074108 (2012).

[15] W. D. Ristenpart, P. G. Kim, C. Domingues, J. Wan, and H. A. Stone, Phys. Rev. Lett. **99**, 234502 (2007).

[16] P. J. Yunker, T. Still, M. A. Lohr, and A. G. Yodh, Nature (London) **476**, 308 (2011).

[17] K. Sefiane and C. A. Ward, Adv. Colloid Interface Sci. **134–135**, 201 (2007).

[18] T. M. Squires and S. R. Quake, Rev. Mod. Phys. **77**, 977 (2005).

[19] F. Mugele, J. C. Baret, and D. Steinhauser, Appl. Phys. Lett. **88**, 204106 (2009).

[20] M. R. Bringer, C. J. Gerdts, H. Song, J. D. Tice, and R. F. Ismagilov, Philos. Trans. R. Soc. London Ser. Math. Phys. Eng. Sci. **362**, 1087 (2004).

[21] A. Rida and M. A. M. Gijs, Anal. Chem. **76**, 6239 (2004).

[22] T. Frommelt, M. Kostur, M. Wenzel-Schäfer, P. Talkner, P. Hänggi, and A. Wixforth, Phys. Rev. Lett. **100**, 034502 (2008).

[23] F. Mugele, A. Staicu, R. Bakker, and D. van den Ende, Lab Chip **11**, 2011 (2011).

[24] P. Roach, N. J. Shirtcliffe, and M. I. Newton, Soft Matter **4**, 224 (2008).

[25] S. Dash, M. T. Alt, and S. V. Garimella, Langmuir **28**, 9606 (2012).

[26] S. A. Kulinich and M. Farzaneh, Appl. Surf. Sci. **255**, 4056 (2009).

[27] S. Dash and S. V. Garimella, Langmuir **29**, 10785 (2013).

[28] S. Dash and S. V. Garimella, Phys. Rev. E **89**, 042402 (2014).

[29] Á. G. Marín, H. Gelderblom, A. Susarrey-Arce, A. van Houselt, L. Lefferts, J. G. E. Gardeniers, D. Lohse, and J. H. Snoeijer, Proc. Natl. Acad. Sci. USA **109**, 16455 (2012).

[30] M. Dicuangco, S. Dash, J. A. Weibel, and S. V. Garimella, Appl. Phys. Lett. **104**, 201604 (2014).

[31] D. Tam, V. von Arnim, G. H. McKinley, and A. E. Hosoi, J. Fluid Mech. **624**, 101 (2009).

[32] R. M. Pope and E. S. Fry, Appl. Opt. **36**, 8710 (1997).

[33] G. Minor, P. Oshkai, and N. Djilali, Meas. Sci. Technol. **18**, L23 (2007).

[34] X. Xu, J. Luo, and D. Guo, Langmuir **26**, 1918 (2010).

[35] Z. Pan, S. Dash, J. A. Weibel, and S. V. Garimella, Langmuir **29**, 15831 (2013).

[36] See Supplemental Material at http://link.aps.org/supplemental/10.1103/PhysRevE.90.062407 for videos of flow behavior inside evaporating droplets and dye mixing patterns.

[37] G. Müller, G. Neumann, and W. Weber, J. Cryst. Growth **70**, 78 (1984).

[38] R. Touihri, H. B. Hadid, and D. Henry, Phys. Fluids **11**, 2078 (1999).

[39] G. Neumann, J. Fluid Mech. **214**, 559 (1990).

[40] C. T. Culbertson, S. C. Jacobson, and J. Michael Ramsey, Talanta **56**, 365 (2002).